Generation of Superponderomotive Electrons in Multipicosecond Interactions of Kilojoule Laser Beams with Solid-Density Plasmas

A. Sorokovikova,[1] A. V. Arefiev,[2] C. McGuffey,[1,*] B. Qiao,[1] A. P. L. Robinson,[3] M. S. Wei,[4] H. S. McLean,[5] and F. N. Beg[1,†]

[1]Center for Energy Research, University of California, San Diego, California 92093, USA
[2]Institute for Fusion Studies, The University of Texas, Austin, Texas 78712, USA
[3]Central Laser Facility, STFC Rutherford-Appleton Laboratory, Didcot OX11 0QX, United Kingdom
[4]General Atomics, San Diego, California 92186, USA
[5]Lawrence Livermore National Laboratory, Livermore, California 94511, USA

(Received 28 August 2014; revised manuscript received 9 March 2016; published 12 April 2016)

The interaction of a multipicosecond, kilojoule laser pulse with a surface of a solid target has been shown to produce electrons with energies far beyond the free-electron ponderomotive limit $m_e c^2 a_0^2/2$. Particle-in-cell simulations indicate that an increase in the pulse duration from 1 to 10 ps leads to the formation of a low-density shelf (about 10% of the critical density). The shelf extends over 100 μm toward the vacuum side, with a nonstationary potential barrier forming in that area. Electrons reflected from the barrier gain superponderomotive energy from the potential. Some electrons experience an even greater energy gain due to ponderomotive acceleration when their "dephasing rate" $R = \gamma - p_x/m_e c$ drops well below unity, thus increasing acceleration by a factor of $1/R$. Both 1D and 2D simulations indicate that these mechanisms are responsible for the generation of extensive thermal distributions with $T_e > 10$ MeV and a high-energy cutoff of hundreds of MeV.

DOI: 10.1103/PhysRevLett.116.155001

A laser-plasma interaction (LPI) at relativistic intensities ($>10^{18}$ W/cm^2) offers an efficient source of fast electrons with an energy above tens of MeV, which is of fundamental interest for a range of applications including accelerator science [1], laboratory astrophysics, and inertial fusion energy [2]. Relativistic LPIs in low-density plasmas have a notable ability to produce high-energy electrons through several known mechanisms such as wake-field [3–5] and direct laser accelerations [6].

However, solid target interaction with such a laser is complex, spanning several orders of magnitude difference in the characteristic temporal and spatial scales between solids and low-density preplasma [7–9]. On subpicosecond time scales, if the preplasma scale length is steep (or zero), fast electrons are produced predominantly by relativistic $\mathbf{j} \times \mathbf{B}$ heating [10], resulting in a Boltzmann-like energy distribution [11–13] with a slope temperature close to the ponderomotive scaling $T_p = [(1 + a_0^2)^{1/2} - 1] m_e c^2$ [14] and a maximum energy near the free-electron ponderomotive limit $E_p = m_e c^2 a_0^2/2$ ($a_0 = eE_0/m_e c\omega$ is the laser field amplitude). When a large-scale preplasma [15–17] is created by intrinsic laser prepulses, electrons of energy $>E_p$ can be produced due to stochastic acceleration [18,19]. However, so far, most studies have focused only on subpicosecond laser cases.

High-intensity petawatt laser facilities that deliver multipicosecond kilojoule laser pulses have become available, such as OMEGA-EP [20], LFEX [21], PHELIX [22], and PETAL [23], and NIF-ARC will become available soon [24]. In this new multipicosecond kilojoule regime, the nature of preplasma heavily evolves with time, instabilities and self-generated electromagnetic fields grow significantly; thus, the dynamics of LPI and the characteristics of fast electron generation are inherently different from those in the subpicosecond regime. Considerable preplasma is expected to build up even for a high-contrast laser due to the thermal expansion of electrons, and on multipicosecond time scales the ions also move collectively. Recent particle-in-cell (PIC) simulations [25] demonstrated ~5 ps evolution of a solid target interaction with lasers, but their scope is limited to a steep preplasma density gradient and a low-Z deuterium plasma. The underlying physics of multipicosecond, kilojoule LPI are unexplored.

In this Letter, we report theoretical and numerical studies on plasma dynamics and fast electron generation inherent to multipicosecond LPIs, yet previously unexplored. Our one- and two-dimensional (1D and 2D, respectively) PIC simulations reveal that electrons with energy far exceeding the free-electron ponderomotive limit are produced, and the temperature and maximum energy of these super-high-energy electrons significantly increase as the laser pulse duration increases from 1 to 10 ps. We find that on multipicosecond time scales the electron density distribution self-evolves into a steplike profile jumping from critical density n_c to $\gamma_0 n_c$ [$n_c = \omega^2 m_e/4\pi e^2$ and $\gamma_0 = (1 + a_0^2)^{1/2}$] followed with a long, flat shelf extending to the subcritical region. A deep, broad electrostatic potential

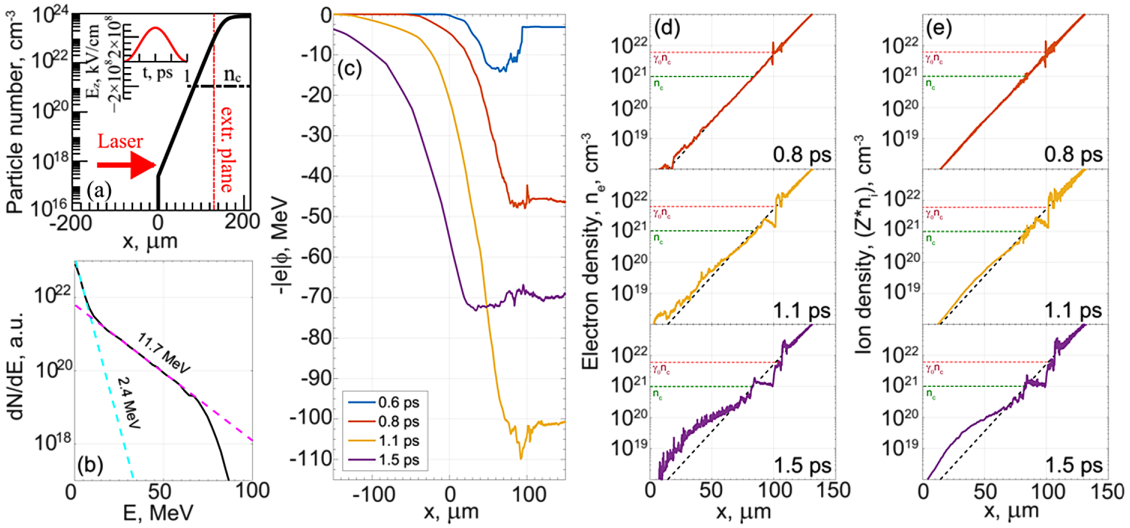

FIG. 1. A 1D PIC simulation of a 1 ps laser interaction with a solid Al target: (a) initial electron density profile; (b) energy spectrum collected at the extraction plane; (c) the electrostatic potentials at various times $t - t_0 = 0.6$, 0.8, 1.1, and 1.5 ps; (d),(e) the corresponding electron and ion density profiles at times as indicated.

profile is induced in the shelf. We prove that the presence of this shelf and the colocated potential are responsible for the energetic electrons. Particle tracing in the simulation and an analytical model have explained that the evolving potential itself imparts significant energy to some electrons and that further acceleration results from the potential's reduction of the electrons' dephasing rate $R = \gamma - p_x/m_e c < 1$ [26,27]. Since the duration and volume in which the antidephasing occurs increase with pulse duration, the number and energy of superponderomotive electrons increase. We show that the antidephasing acceleration occurs even when multidimensional effects are included.

One-dimensional simulations have been carried out using the PIC code EPOCH [28]. We choose a simulation domain spanning $[-600, 200]$ μm in x with 64 000 cells. The corresponding time step allows us to correctly resolve the dynamics of the accelerated electrons [29]. All sides of the domain have an open boundary condition which allows particles and fields to leave the domain freely. One thousand electrons and 100 Al^{13+} ions per cell are loaded for a solid (2.7 g/cm^3) aluminum target, which represent different numbers of real particles. The initial electron density is $n_e(x) = Zn_{\text{solid}}/\{1 + \exp[-(x - x_0)/L]\}$, shown in Fig. 1(a), where $L = 10$ μm, $Z = 13$, and $x_0 = 150$ μm. The preplasma extends to $x = 0$, reaching 2.4×10^{17} cm^{-3}. The space $x < 0$ is vacuum, allowing room for thermal expansion of plasma electrons throughout multipicoseconds. Initial electron and ion temperatures are both chosen to be 100 eV. A 1 μm wavelength laser with the peak intensity 10^{20} W/cm^2 ($a_0 = 8.54$) is injected at $x = -600$ μm and reaches the plasma at $x = 0$ at $t \equiv t_0$, which is 2.0 ps for all 1D simulations here. The laser field E_z has the temporal profile $\sin^2(\pi t/\tau)$, where τ is the laser pulse duration.

The extraction plane diagnostic, which collects the information of passing particles, is located at $x = 130$ μm.

The spectrum [Fig. 1(b)] clearly indicates two slope temperature components: the ponderomotive one with 2.4 MeV and the super-high-energy one with 11.7 MeV, with maximum energy 90 MeV, far exceeding the free-electron ponderomotive limit ~25 MeV.

Figures 1(c)–1(e) plot, respectively, the self-generated electrostatic potentials, electron, and ion densities at times $t - t_0 = 0.6$, 0.8, 1.1, and 1.5 ps (the laser pulse duration is $\tau = 1$ ps). The potential is calculated from zero at the left boundary and integrating over the electric field. For this pulse duration, new behaviors characteristic to multipicosecond kilojoule LPIs are onset. First, the strong laser ponderomotive pressure (30 Gbar at 10^{20} W/cm^2) keeps compressing preplasma electrons at the critical density n_c, which eventually forms a steep critical surface jumping from n_c to $\gamma_0 n_c$. The laser front is depleted here within a skin depth, passing energy to electrons through $\mathbf{j} \times \mathbf{B}$ heating, where the final energy spectrum of these electrons obeys the ponderomotive scaling [14]. Second, a flat shelf electron density profile is self-formed within the near-critical region ($0.1n_c < n_e < n_c$) [see Fig. 1(d)]. Note that the ions also move in the 1 ps time scale [see Fig. 1(e)]. Third, corresponding to this step-function-like density profile, a deep, broad electrostatic potential profile [Fig. 1(c)] is induced, which evolves with time, and electrons in the near-critical region oscillate inside the potential.

To analyze the mechanism of the above super-high-energy electron production, we consider a 1D model for single electron motion in the presence of laser fields $\mathbf{E}$ and $\mathbf{B}$ and an electrostatic potential φ as $d\mathbf{p}/dt = -e(\mathbf{E} + \mathbf{v} \times \mathbf{B}/c) + e\nabla\phi$ and $d\gamma/dt = -\mathbf{v} \cdot \mathbf{E} + \mathbf{v} \cdot \nabla\varphi$, where $\mathbf{p} = \gamma m_e \mathbf{v}$ and $\gamma = (1 + p^2/m_e^2 c^2)^{1/2}$ are the electron momentum and relativistic factor, respectively. We assume the laser is a planar wave with normalized vector potential $Ae_z = a_0 \cos(\omega t - k_x x)e_z$. After differentiating,

we can obtain an electron's motion in the transverse and longitudinal directions, respectively, as $dp_z/d\tau_c = d(eA)/d\tau_c$ and $d(\gamma - p_x/m_e c)/d\tau_c = -(e/m_e c)\partial\phi/\partial x$, where $\tau_c = t - x/c$. If assuming that the electron is initially at rest, we get a key integral of the electron transverse motion as $p_z = eA$. Furthermore, if $\varphi = 0$, another integral of electron longitudinal motion can be found: $R = \gamma - p_x/m_e c = 1$. In the low-density regions where most acceleration takes place, the laser phase velocity is nearly c, and R represents the electron's dephasing rate [30]. The maximum energy electrons can gain in this case is $E_p = m_e c^2 a_0^2/2$.

However, during a multipicosecond LPI, a deep, broad electrostatic potential profile is induced [Fig. 1(c)], which leads to $R \neq 1$. Therefore, we can write an electron's equation of longitudinal motion as

$$\frac{dp_x}{dt} = \frac{1}{R}\frac{e^2 A}{m_e c}\frac{dA}{dt} + e\frac{\partial\phi}{\partial x}, \tag{1}$$

$$R = 1 - \frac{e}{m_e c}\int \frac{\partial\phi}{\partial x} d\tau_c = 1 - \frac{e}{m_e c}\int \frac{\partial\phi}{\partial x}\left(1 - \frac{v_x}{c}\right) dt. \tag{2}$$

Equations (1) and (2) together describe the dynamics of super-high-energy electron production in the near-critical shelf region during multipicosecond LPI, where a deep electrostatic potential profile develops. The effect of the induced electrostatic potential barrier is not only directly awarding additional energy $e(\delta\phi)$ to electrons, but also linked with the laser ponderomotive acceleration through the dephasing rate R. When electrons oscillate inside the potential profile, they experience antidephasing ($\partial\phi/\partial x > 0$, $R < 1$) in its left half and dephasing ($\partial\phi/\partial x < 0$, $R > 1$) in its right half. That respectively results in acceleration or deceleration under the laser ponderomotive force by a factor of $1/R$.

As seen in Fig. 1(c), because the plasma expansion dominates on the vacuum side, the left half of the potential barrier is much wider and deeper than the right. So electrons always experience longer and larger antidephasing than dephasing. From the viewpoint of a nonstationary Hamiltonian theory [31–34], antidephasing (resulting in a high-energy electron acceleration) may be interpreted as a reduction of the "moving-frame" Hamiltonian $H(\tau_c, x) = m_e c^2 \gamma_e - c p_x - e\phi$, where $\gamma_e = (1 + p^2/m_e^2 c^2 + a_0^2/2)^{1/2}$.

Note that the profile of the potential evolves during the multipicosecond LPI. A broader, deeper left wall and a sharper right wall potential should produce more super-high-energy electrons, because it creates a large volume for antidephasing. Note that the leftmost side of the potential barrier in Fig. 1 can directly accelerate electrons.

Figure 2 displays information from recorded trajectories of individual particles. Figure 2(a) shows the time histories of work done by electric field components on two particles exemplifying superhigh acceleration ("H," top) and $\mathbf{j} \times \mathbf{B}$ heating ("L," bottom). Their momentum and dephasing rate time histories are shown in Figs. 2(b) and 2(c), respectively. Both electrons experienced large antidephasing (R decreases to $\ll 1$) from the left of the potential barrier, which began forming by $t - t_0 \approx 0.6$ ps [Fig. 1(c)]. However, particle H first moved toward the vacuum side and then experienced rapid acceleration and antidephasing throughout its transit from $x = 10$ μm until it reached a maximum energy at $x = 70$ μm. As a result, it achieved a final $p_x/m_e c$ of 180, 4.5 times greater than particle L and 3.5 times the free-electron ponderomotive limit. Particle L was accelerated with minimal work done by the electrostatic potential, and antidephasing coincided with

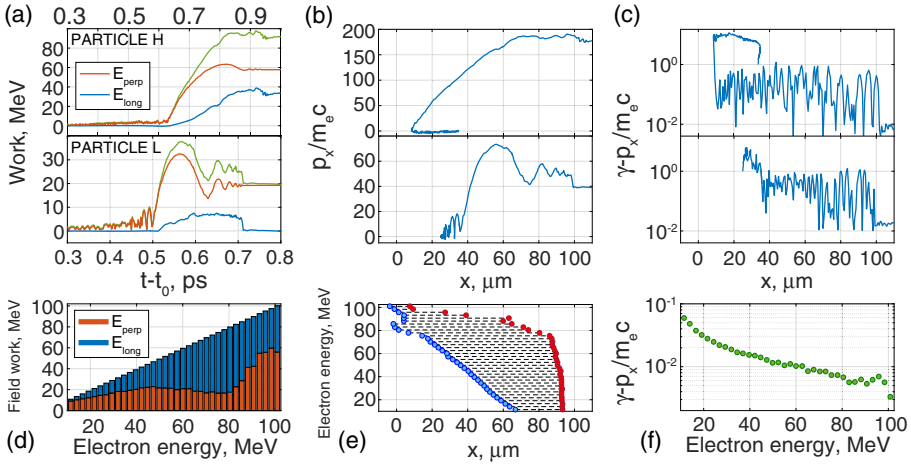

FIG. 2. (a) The work done on two characteristic test particles by longitudinal electric fields such as the electrostatic potential (blue curve), by transverse fields (brown curve), and total (green curve). (b),(c) The momentum $p_x(t)$ and dephasing rate $R(t)$ for the same electrons. (d) The average work done by each field component on tracked electrons binned by their final energy. (e) Energy bins of tracked electrons versus their average original positions (red) and farthest extent to the left (blue). (f) The average final dephasing rate R of fast electrons binned by their final energies.

acceleration only briefly between $x = 35$ and 55 μm, resulting in a much lower final $p_x/m_e c$ of 40.

Figure 2(d) displays the work done by the different field components averaged over all test particles binned by their final energy. The lowest-energy particles gain energy predominantly by the perpendicular (laser) field, and intermediate energies ($10 < E < 80$ MeV) gain nearly the same quantity (10–20 MeV) from the laser field. The highest-energy electrons (>80 MeV) gain significant energy from the longitudinal field (electrostatic potential) and notably experience work greatly exceeding the free-electron ponderomotive limit by the laser field. Figure 2(e) plots the average original positions and leftmost extents of eventual fast electrons. The electrons reaching low and modest energies originate from the steep critical surface, and energy correlates with long travel into the shelf region. The super-high-energy ones ($E > 80$ MeV) come from the shelf region far from the critical surface. From Fig. 2(f)—the final dephasing rate R of fast electrons versus their energy—we can also see that super-high-energy electrons do come from the antidephasing mechanism with final $R \ll 1$.

The evolution of the electrostatic potential profile plays a key role in the antidephasing mechanism. Therefore, electron acceleration in multipicosecond LPIs heavily depends on the laser pulse durations. Figures 3(a)–3(d) plot electron density profiles late in the interactions for $\tau = 1$, 3, 5, and 10 ps, respectively. The longer pulse durations significantly enhance both the density steepening and the extension of the long shelf profile. Correspondingly, a much wider and deeper potential barrier is self-formed for longer τ [Fig. 3(f)], leading to longer and greater antidephasing electron acceleration. The temperature and maximum energy of electrons are increased by extension of the laser pulse; see Fig. 3(e). On the other hand, the low-energy spectrum shapes are similar, due to the fixed intensity.

To check if the antidephasing mechanism is extant in a multidimensional case, 2D simulations were conducted in a system domain spanning $x = [-170, 130]$ μm in the longitudinal direction (18 000 cells) resulting in $t_0 = 567$ fs and $y = [-30, 30]$ μm in the transverse direction (1200 cells). The density profiles were the same as the 1D simulations with 20 electrons and five ions per cell. The laser had a transverse Gaussian profile with 10.6 μm FWHM and durations $\tau = 1$ and 5 ps. Figures 4(a) and 4(b) plot electron density distributions and their longitudinal profiles [Fig. 4(c)] for both durations. The intense laser propagates deeply into the plasma, reaching the relativistic critical density of 10^{22} cm^{-3}, and a quasistatic lower-density (10^{20}–10^{21} cm^{-3}) channel is created near the x axis. Inside the channel, the radial charge separation electric field balances the radial expelling ponderomotive force, allowing fast electrons to be accelerated longitudinally via dynamics similar to the 1D cases. Both the critical density steepening and the self-formation of the near-critical shelf can still be observed inside the channel [Fig. 4(c)], inducing a broad electrostatic potential profile [Fig. 4(d)]. The previously discussed acceleration mechanisms still occur in 2D geometry.

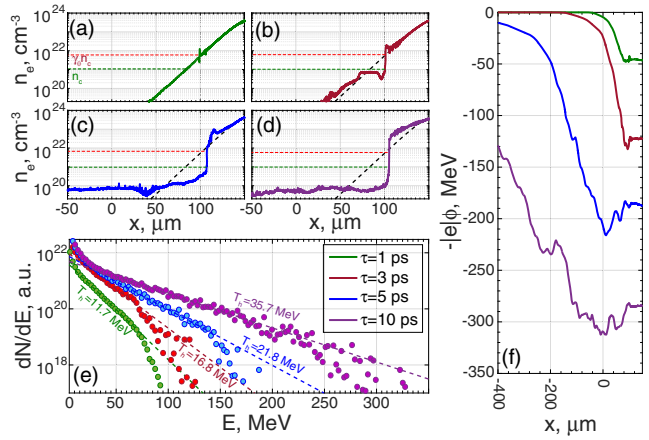

FIG. 3. (a)–(d) Electron density profiles at $t - t_0 = (0.8, 1.8, 4.2, 6.7)$ ps for laser durations $\tau = (1, 3, 5, 10)$ ps, respectively. (e) Time-integrated energy spectra of fast electrons entering the solid; (f) corresponding electrostatic potential profiles at the same times as (a)–(d).

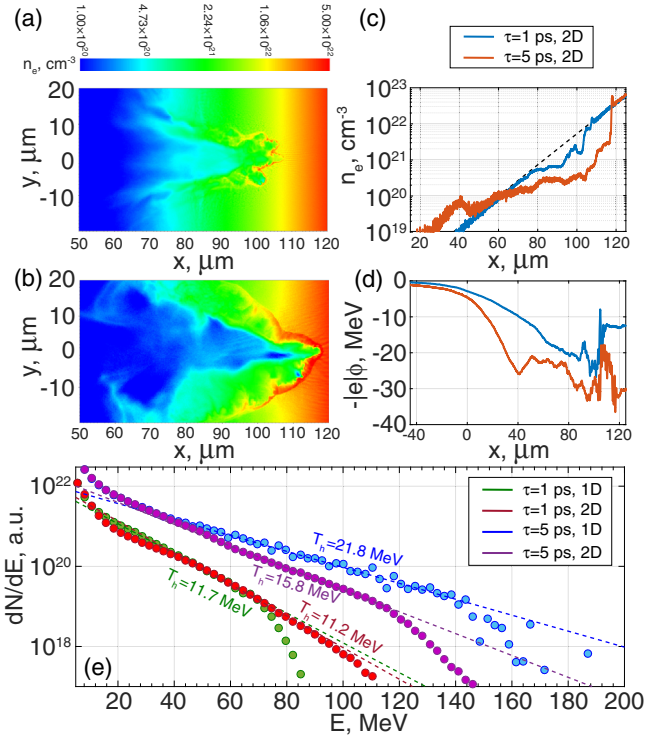

FIG. 4. The 2D PIC simulation results: electron density in 1 (a) and 5 ps (b) cases at $t - t_0 = 0.95$ and 3.05 ps, respectively; (c) axial electron density profiles inside the channel of (a) and (b); (d) corresponding electrostatic potential profiles inside the channel; (e) time-integrated electron energy spectra, in comparison with the previous 1D results.

Figure 4(e) shows the time-integrated electron energy spectra in 2D simulations. The results are consistent with the 1D results: A large number of super-high-energy electrons are produced, and their temperature and maximum energy increase for a longer pulse duration. The difference between 1D and 2D results for 5 ps at the highest energies can be attributed to a weaker potential barrier [compare Fig. 4(d) to Fig. 3(f)] due to an additional degree of freedom allowed for plasma expansion, and the strong potential is restricted to the axis, affecting fewer particles.

There are other enhanced acceleration mechanisms [35] that might also be at work in multidimensional cases. In principle, there are three factors leading to antidephasing: (a) the electrostatic potential barrier discussed here, (b) the electrostatic field in the plasma channel [26,27], and (c) the reflected electromagnetic wave.

In summary, we have studied intense LPI and fast electron generation in the multipicosecond kilojoule scale regime. It is found that a substantial number of superponderomotive electrons are produced and their temperature and maximum energy significantly increase with the laser pulse duration (1–10 ps). The electrostatic potential barrier, which builds up on the subcritical side throughout the multipicosecond interaction, increases electron energy through electrostatic acceleration and enhances the ponderomotive acceleration via the antidephasing mechanism. Both effects contribute to the generation of numerous superponderomotive electrons with temperatures >10 MeV and an energy cutoff of hundreds of MeV.

This work was performed under the auspices of U.S. DOE under Contracts No. DE-NA0000870, No. DE-FG02-05ER54834, and No. DE-FC02-04ER54789. Simulations were performed using the EPOCH code (developed under United Kingdom EPSRC Grants No. EP/G054940/1, No. EP/G055165/1, and No. EP/G056803/1) using HPC resources provided by the TACC at the University of Texas. A. V. A. was supported by the U.S. DOE through Agreements No. DE-NA0002008 and No. DE-FG02-04ER54742.

*Corresponding author.
cmcguffey@ucsd.edu
†fbeg@ucsd.edu

[1] T. Tajima and J. M. Dawson, Phys. Rev. Lett. **43**, 267 (1979).
[2] J. D. Lindl, Phys. Plasmas **2**, 3933 (1995).
[3] G. A. Mourou, T. Tajima, and S. V. Bulanov, Rev. Mod. Phys. **78**, 309 (2006).
[4] E. Esarey, C. B. Schroeder, and W. P. Leemans, Rev. Mod. Phys. **81**, 1229 (2009).
[5] V. Malka, Phys. Plasmas **19**, 055501 (2012).
[6] A. Pukhov, Z. M. Sheng, and J. Meyer-ter-Vehn, Phys. Plasmas **6**, 2847 (1999).
[7] W. Theobald *et al.*, Phys. Plasmas **13**, 043102 (2006).
[8] T. Ma *et al.*, Phys. Rev. Lett. **108**, 115004 (2012).
[9] A. G. MacPhee *et al.*, Phys. Rev. Lett. **104**, 055002 (2010).
[10] W. L. Kruer and K. Estabrook, Phys. Fluids **28**, 430 (1985).
[11] M. Sherlock, Phys. Plasmas **16**, 103101 (2009).
[12] T. Kluge, T. Cowan, A. Debus, U. Schramm, K. Zeil, and M. Bussmann, Phys. Rev. Lett. **107**, 205003 (2011).
[13] J. May, J. Tonge, F. Fiuza, R. A. Fonseca, L. O. Silva, C. Ren, and W. B. Mori, Phys. Rev. E **84**, 025401 (2011).
[14] S. C. Wilks, W. L. Kruer, M. Tabak, and A. B. Langdon, Phys. Rev. Lett. **69**, 1383 (1992).
[15] A. J. Kemp, Y. Sentoku, and M. Tabak, Phys. Rev. E **79**, 066406 (2009).
[16] B. S. Paradkar, M. S. Wei, T. Yabuuchi, R. B. Stephens, M. G. Haines, S. I. Krasheninnikov, and F. N. Beg, Phys. Rev. E **83**, 046401 (2011).
[17] Y. Ping *et al.*, Phys. Rev. Lett. **109**, 145006 (2012).
[18] B. S. Paradkar, S. I. Krasheninnikov, and F. N. Beg, Phys. Plasmas **19**, 060703 (2012).
[19] Z. M. Sheng, K. Mima, Y. Sentoku, M. S. Jovanović, T. Taguchi, J. Zhang, and J. Meyer-ter-Vehn, Phys. Rev. Lett. **88**, 055004 (2002).
[20] D. N. Maywar *et al.*, J. Phys. Conf. Ser. **112**, 032007 (2008).
[21] N. Miyanaga *et al.*, J. Phys. IV **133**, 81 (2006).
[22] V. Bagnoud *et al.*, Appl. Phys. B **100**, 137 (2010).
[23] D Batani *et al.*, Phys. Scr. **2014**, 014016 (2014).
[24] J. Crane *et al.*, J. Phys. Conf. Ser. **244**, 032003 (2004).
[25] A. J. Kemp and L. Divol, Phys. Rev. Lett. **109**, 195005 (2012).
[26] A. V. Arefiev, B. N. Breizman, M. Schollmeier, and V. N. Khudik, Phys. Rev. Lett. **108**, 145004 (2012).
[27] A. P. L. Robinson, A. V. Arefiev, and D. Neely, Phys. Rev. Lett. **111**, 065002 (2013).
[28] T. D. Arber, K. Bennett, C. S. Brady, A. Lawrence-Douglas, M. G. Ramsay, N. J. Sircombe, P. Gillies, R. G. Evans, H. Schmitz, A. R. Bell, and C. P. Ridgers, Plasma Phys. Controlled Fusion **57**, 113001 (2015).
[29] A. V. Arefiev, G. E. Cochran, D. W. Schumacher, A. P. L. Robinson, and G. Chen, Phys. Plasmas **22**, 013103 (2015).
[30] A. P. L. Robinson, A. V. Arefiev, and V. N. Khudik, Phys. Plasmas **22**, 083114 (2015).
[31] P. Mora, Phys. Fluids B **4**, 1630 (1992).
[32] S. A. Yi, V Khudik, S. Y. Kalmykov, and G. Shvets, Plasma Phys. Controlled Fusion **53**, 014012 (2011).
[33] S. Y. Kalmykov, B. A. Shadwick, A. Beck, E. Lefebvre, S. A. Yi, V. Khudik, and M. C. Downer, AIP Conf. Proc. **1299**, 174 (2010).
[34] S. Y. Kalmykov, A. Beck, S. A. Yi, V. N. Khudik, M. C. Downer, E. Lefebvre, B. A. Shadwick, and D. P. Umstadter, Phys. Plasmas **18**, 056704 (2011).
[35] A. V. Arefiev, V. N. Khudik, and M. Schollmeier, Phys. Plasmas **21**, 033104 (2014).